Experimental and numerical investigation to rationalize both near-infrared and mid-infrared spontaneous emission in Pr^{3+} doped selenide-chalcogenide fiber

Slawomir Sujecki[1]*, Lukasz Sojka[1], Elzbieta Beres-Pawlik[1], Krzysztof Anders[2], Ryszard Piramidowicz[2], Zhuoqi Tang[3], David Furniss[3], Emma Barney[3], Trevor Benson[3] and Angela Seddon[3]

[1]Wroclaw University of Science and Technology, Faculty of Electronics, Janiszewskiego 11/17, 50-372 Wroclaw, Poland;
[2]Warsaw University of Technology, Institute of Microelectronics and Optoelectronics, Koszykowa 75, 00-662 Warsaw, Poland;
[3]The University of Nottingham, Faculty of Engineering, University Park, NG7 2RD Nottingham, UK;

Corresponding author

Slawomir Sujecki

Wroclaw University of Science and Technology, Faculty of Electronics,

Janiszewskiego 11/17, 50-372 Wroclaw, Poland;

tel. +48-71-3204588

e-mail: slawomir.sujecki@pwr.edu.pl

Abstract: This contribution reports on detailed experimental and numerical investigations of both near-infrared (NIR) and mid-infrared (MIR) photoluminescence obtained in praseodymium trivalent ion doped chalcogenide-selenide glass fiber. The experimental analysis allows for the identification of the radiative transitions within the praseodymium ion energy level structure to account for the photoluminescent behavior. Numerical analysis is carried out using the rate equations' approach to calculate the level populations. The numerical analysis provides further insight into the nature of the radiative transitions in the Pr^{3+} ion doped chalcogenide-selenide glass and allows for the identification of the electronic transitions, which contribute to the observed photoluminescence. The numerical results agree well with the experimental results.

Keywords: chalcogenide glass fibers; lanthanide doped fibers; optical fiber modelling

1. Introduction

Mid-infrared (MIR) fiber sources emitting at wavelengths in the range 3 μm to 6 μm have many applications in remote sensing, medicine and defense [1]. However, in order to access these wavelengths using dielectric hosts, low phonon materials are needed. Among the most promising materials for this wavelength region are chalcogenide glasses [2-5]. Chalcogenide glasses possess sufficient rare earth ion solubility, high refractive index, low phonon energy and can be drawn into ~~a~~ small-core fiber [6]. These characteristics make chalcogenide glasses a promising host material for rare-earth ions [6-10]. Recent publications show that there is a particularly large interest in the mid-infrared photoluminescence from Pr^{3+} doped low phonon materials [11-17]. This is because a Pr^{3+} ion dopant in a chalcogenide glass has a high pump absorption cross-section [18], and also because it can be pumped with commercially available laser diodes operating at 1.55 μm and 1.94 μm. Many devices for MIR applications based on

chalcogenide glass fibers have been already demonstrated, which include supercontinuum sources, Raman lasers and compact sensing devices [19-25]. Also, an extensive effort has been invested into the design and modelling of MIR fiber-based and waveguide-based incoherent light sources based on Pr^{3+} ion doped chalcogenide glass fibers [26-31].

Despite the large number of publications on Pr^{3+} ion doped chalcogenide glass optical properties, there is still a need for further investigation of this topic. This is primarily because MIR Pr^{3+} ion doped chalcogenide glass fiber lasing has not been achieved yet. The analysis of MIR emission from Pr^{3+} ions is complicated by the fact that several transitions, *e.g.* ($^3F_4$,$^3F_3 \rightarrow$ $^3F_2$,$^3H_6$), ($^3F_2$,$^3H_6 \rightarrow$ $^3H_5$) and ($^3H_5 \rightarrow$ $^3H_4$), can contribute to mid-infrared emission at around 4.7 μm. Additionally, the energy gap between manifolds ($^3F_4$,$^3F_3$) and ($^3F_2$,$^3H_6$) is small and hence it is difficult to determine accurately lifetimes for these transitions. Lastly, it should be considered that there still remains underlying extrinsic absorption in the active fiber region due to unwanted anionic contamination in the glass host; this can lead to the presence of an extrinsic high phonon energy transitions competing to deplete non-radiatively the Pr^{3+} excited states as explained in [32].

In this contribution, we re-investigate in detail data on the photoluminescence from Pr^{3+} chalcogenide fiber, using both experimental and numerical methods.

2. Methods and Materials

For the experimental work, usually 500 ppmw (parts per million by weight) Pr^{3+}-doped GeAsGaSe bulk glass has been made by the melt-quenching route. For the glasses: As (7N Furakawa Denshi; further purified by heating under vacuum), Se (5N Materion; heat treated under vacuum), Ge (5N Cerac), Ga (5N Testbourne Ltd., melting point 29.8°C at 1 atm, i.e. 1.013 x 10^5 Pa) and Pr foil (3N Alfa Aesar) were batched into a purified silica-glass ampoule inside a glove-box (N_2 with < 0.1 ppmw H_2O and < 0.1 ppmw O_2; MBraun). The ampoule sealed under vacuum (10^3 Pa) was then rocked in a resistance furnace (Instron) for 12–14 h/850°C, quenched and chalcogenide glass annealed (Instron) close to its glass transition temperature (Tg). After annealing, the core glass and cladding chalcogenide glass boules were polished, co-extruded to form a step-index preform using an in-house extruder and then the preform was fiber-drawn on a customized Heathway fiber drawing tower, inside a class-10,000 clean room. The 500 ppmw Pr^{3+} -doped GeAsGaSe core glass/GeAsGaSe cladding glass optical fiber had an outside diameter of 250 μm, the length of 60 mm and was not polymer-coated. To the best of our analysis the core diameter was found to be ~224 μm. Further details on the fabrication procedure can be found in [33]. The basic material and optical properties of the fiber used in the experiments have been characterized and discussed in separate publications [6,9].

3. Experimental Results

Fig. 1. shows the schematic diagrams of the measurement setups used for recording of the photoluminescence spectrum and temporal decay. For photoluminescence spectra measurements (Fig. 1a) the signal is collected from the fiber end and delivered to monochromator entrance using a set of Calcium Fluoride lenses, whilst the pump light is provided at the other end of the fiber. Mercury Cadmium Telluride (MCT) photodetector PVI-4TE6 (Vigo Systems) records MIR light intensity. The signal from MCT photodetector is delivered to lock-in amplifier together with the signal from the chopper driver. Post processing of the results is carried out by a personal computer connected with a data acquisition card. In the case of the photoluminescence decay curves, the pumping laser diode is directly modulated by the current drive and illuminates one end of the fiber (Fig. 1b). The signal is collected from

the other end and imaged onto the MCT photodetector. The signal from the MCT photodetector is amplified and provided to an oscilloscope. In order to suppress noise, an averaging over several thousand process realization is performed. In both setups filters are used to suppress the residual pump signal.

a)

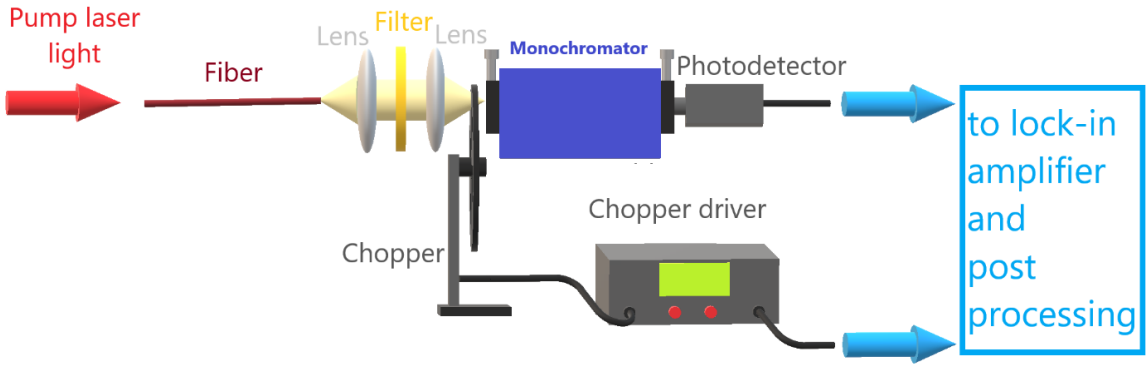

b)

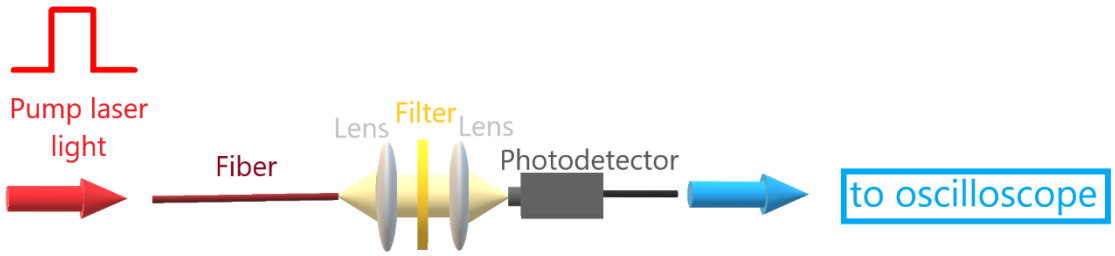

Figure 1. Measurement setup for recording: (a) photoluminescence spectrum; (b) photoluminescence decay.

Fig. 2. shows the simplified energy level diagram of Pr^{3+} ions doped into a chalcogenide glass host. Arrows mark potential transitions, that may occur when pumping into the $^3F_4$ and $^3F_3$ levels. This pumping is achieved by applying a commonly-available laser diode type, operating at a wavelength of ~1450 nm. The wavelength of 1450 nm was selected because low-cost high-power semiconductor lasers operating at this wavelength are readily commercially available. Further the praseodymium ions when doped into a chalcogenide glass have an absorption peak near 1450 nm and the host chalcogenide glass intrinsic absorption loss is relatively low, which helps reducing the heat generation during the optical pumping process. In chalcogenide-selenide glasses, it has been proposed that the energy levels $^3F_4$ and $^3F_3$, and also $^3F_2$ and $^3H_6$, are mutually thermally coupled [3]; these are marked in Fig. 2 with loops each uniting one pair of transitions. Fig. 3a shows the near-infrared (NIR) photoluminescent spectrum spanning the wavelength range from 1.5 μm to 1.7 μm, recorded using a Yokogawa AQ6370D spectrum analyzer. This photoluminescence was collected from the side of the fabricated 500 ppm Pr^{3+} ion doped GeAsGaSe glass fiber sample using a multimode silica fiber with 1 mm core diameter. The chalcogenide fiber sample was illuminated at one end with a multimode laser diode pump operating at 1450 nm. As the cut-off wavelength of the spectrometer was 1700 nm, measurement of the spectrum above this wavelength was suppressed. Nevertheless, as seen in Fig. 2. a broad photoluminescence, stretching from 1500 nm to 1700 nm, is observed. Considering the energy level diagram shown in Fig. 2, this photoluminescence was attributed to the transition ($^3F_4$,$^3F_3$ → $^3H_4$). It is noted that this

wavelength range is relevant to optical telecommunications' applications, particularly the C and L bands.

Interestingly, unlike the transition ($^7F_4 \rightarrow {}^7F_5$) in terbium (III) ions, doped into a chalcogenide-selenide glass, the transition ($^3F_4,^3F_3 \rightarrow {}^3H_4$) in praseodymium (III) ions was not observed here to be suppressed by non-radiative quenching due to intrinsic host phonons between levels ($^3F_3$ and $^3F_2$). This is despite the fact that the energy gap between levels ($^3F_3 \rightarrow {}^3F_2$) for praseodymium (III) is ~1367 cm^{-1} and is similar to that occurring of the ($^7F_4 \rightarrow {}^7F_5$) transition in terbium (III) ions (~1290 cm^{-1}). The intrinsic multiphoton energy of a chalcogenide-selenide host glass is ~300 cm^{-1} [32], therefore for the Pr^{3+}-doped chalcogenide-selenide glass this ($^3F_3 \rightarrow {}^3F_2$) gap of around ~1367 cm^{-1} would require at least 4 host phonons to bridge it successfully. This is on the edge of the generally accepted number 4-6 phonons requirement [32].

Fig. 3b shows the emission spectrum of Pr^{3+}-doped chalcogenide-selenide glass fiber, again end-illuminated with multimode 1450 nm radiation, recorded from 2.0 μm to 2.6 μm using a monochromator, coupled with an extended InGaAs photodetector. Lock-in detection was used to improve the signal-to-noise ratio. The photoluminescence was collected from the other end of the fiber whereby the residual pump light was suppressed using a germanium filter (Fig. 1a). It is noted that reabsorption may influence the results in such measurement configuration. Thus the discussion of this phenomenon in lanthanide doped chalcogenide glass fibers is given in a separate contribution [34]. According to the energy level diagram in Fig. 2, this photoluminescence is concluded to be associated with overlapping transitions ($^3F_4,^3F_3 \rightarrow {}^3H_5$) and ($^3F_2,^3H_6 \rightarrow {}^3H_4$). It is noted, however, that this spectrum is suppressed on the long wavelength side by the detector bandwidth limitation. Nonetheless, the results shown in Fig. 3b confirm the presence of broad photoluminescence in the range: 2.0 μm - 2.6 μm.

Fig. 4 shows the photoluminescence spectrum recorded for the wavelength range spanning from 3.6 μm to 6 μm. Again, a multimode laser diode operating at 1450 nm was used to illuminate one end of the fiber. The photoluminescence was collected from the other fiber-end and delivered to a monochromator using a pair of calcium fluoride f = 25 mm lenses and a long-pass filter with cut-on wavelength of 3600 nm. Again lock-in amplification was used to improve the signal-to-noise ratio. Considering the energy level diagram (Fig. 1), this photoluminescence is attributed to transitions ($^3F_2,^3H_6 \rightarrow {}^3H_5$) and ($^3H_5 \rightarrow {}^3H_4$). However, in principle the transition ($^3F_4,^3F_3 \rightarrow {}^3F_2,^3H_6$) might also contribute to emission within 3.5 μm to 6 μm wavelength range. These spectroscopic measurements confirm that Pr^{3+}-doped chalcogenide-selenide fiber is a potential candidate for a realization of broadly tunable mid-infrared fiber lasers, fiber amplifiers and spontaneous emission sources.

Figure 5 presents the photoluminescence (PL) decay characteristic of the 500 ppmw Pr^{3+} doped Ge-As-Ga-Se fiber, measured using the extended InGaAs photodetector in the spectral wavelength range between 2.0 and 2.6 μm. The 1450 nm multimode laser was directly modulated from the current source with a repetition frequency not exceeding 10 Hz. Consistently with the results presented in Fig. 3b a least squares fit of the measured results was performed using a sum of two exponential functions. This procedure yielded a fast decay with time constant: $\tau = 0.236$ ms, which can be attributed to the ($^3F_4,^3F_3 \rightarrow {}^3H_5$) transition and a slow decay with $\tau = 3.24$ ms that is a contribution from the ($^3F_2,^3H_6 \rightarrow {}^3H_4$) transition (Fig. 6). Subsequently using the same optical set-up, and a mid-infrared photodetector, a photoluminescence decay was recorded for the 3600-6000 nm band (Fig. 7). The measured results were then fitted with a single exponential function (*cf.* Fig. 5). Therefore, it can be concluded that this decay curve may be mainly attributed to the ($^3H_5 \rightarrow {}^3H_4$) transition. The origin of this photoluminescence decay is further explored in the next section using a numerical model.

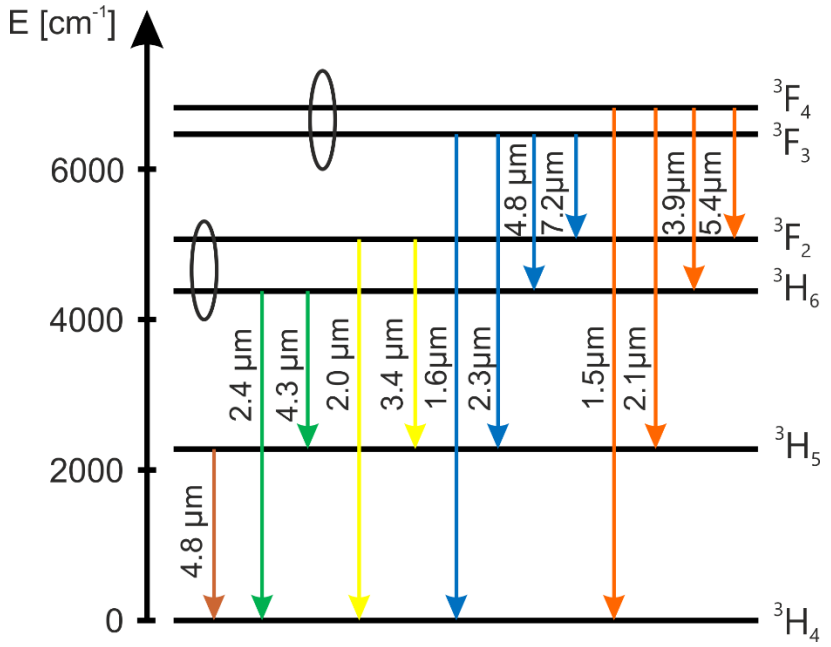

Figure 2. Simplified energy level diagram for Pr^{3+} in chalcogenide glass with transitions relevant to the discussion identified.

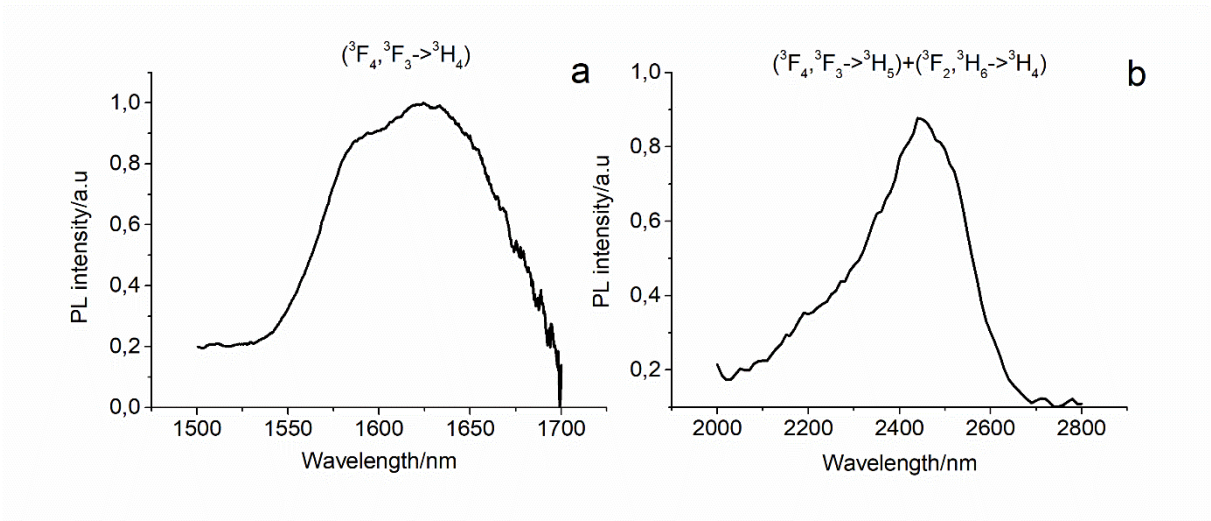

Figure 3. Measured emission of 500 ppmw Pr^{3+}-doped GeAsGaSe large-core step-index fiber: (a) from 1.5 to 1.7 µm, which is attributed to the transition ($^3F_4$,$^3F_3$ → $^3H_4$); (b) from 2.0 to 2.6 µm, which is attributed to two different transitions: ($^3F_4$,$^3F_3$ → $^3H_5$) and ($^3F_2$,$^3H_6$ → $^3H_4$); (see Fig. 1).

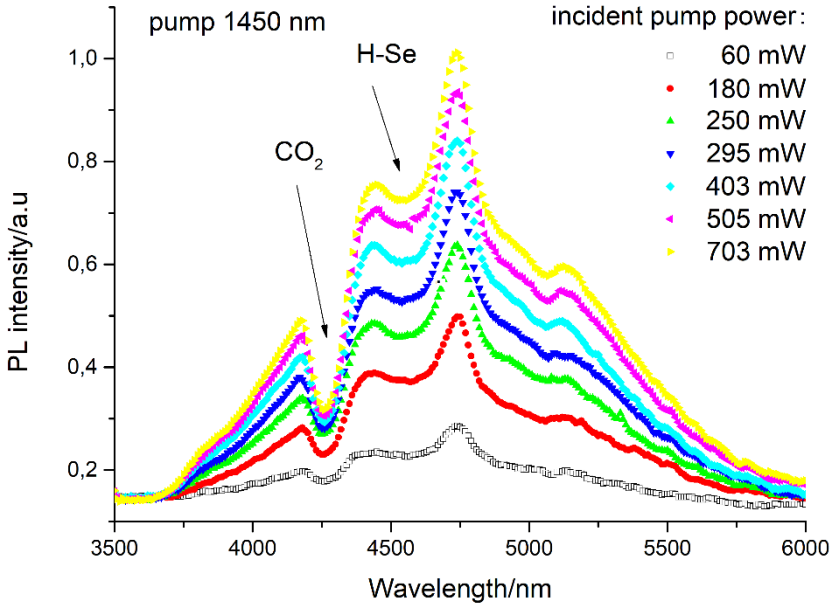

Figure 4. Measured mid-infrared emission spectrum of the 500 ppmw Pr^{3+}-doped GeAsGaSe large-core step-index fiber using a lock-in and MCT detector with preamplifier and 1450 nm CW laser excitation recorded for different pump powers. The emission intensities were not corrected for system response.

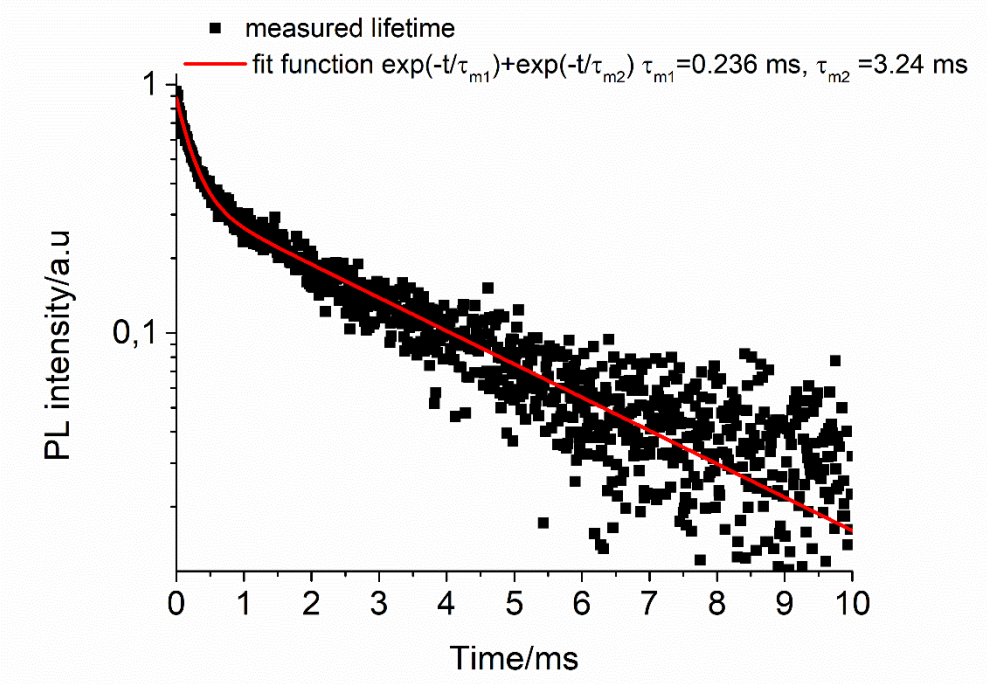

Figure 5. Measured luminescence decay at 2.4 μm using extended InGaAs detector in 500 ppmw Pr^{3+}-doped GeAsGaSe large-core step-index fiber after laser excitation at 1450 nm. The red plot indicates the best fit to a sum of two exponential functions.

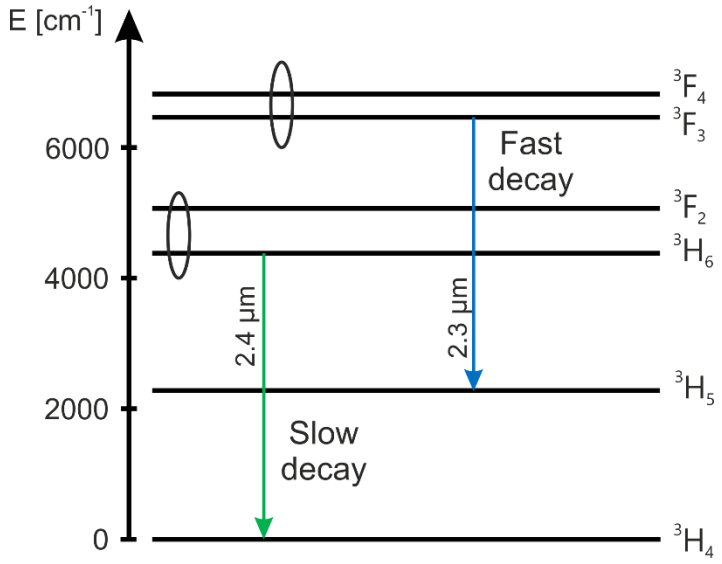

Figure 6. Energy level diagram of Pr^{3+} indicating the most probable transitions attributable to the decay curve recorded at a wavelength of 2.4 µm (Fig. 5).

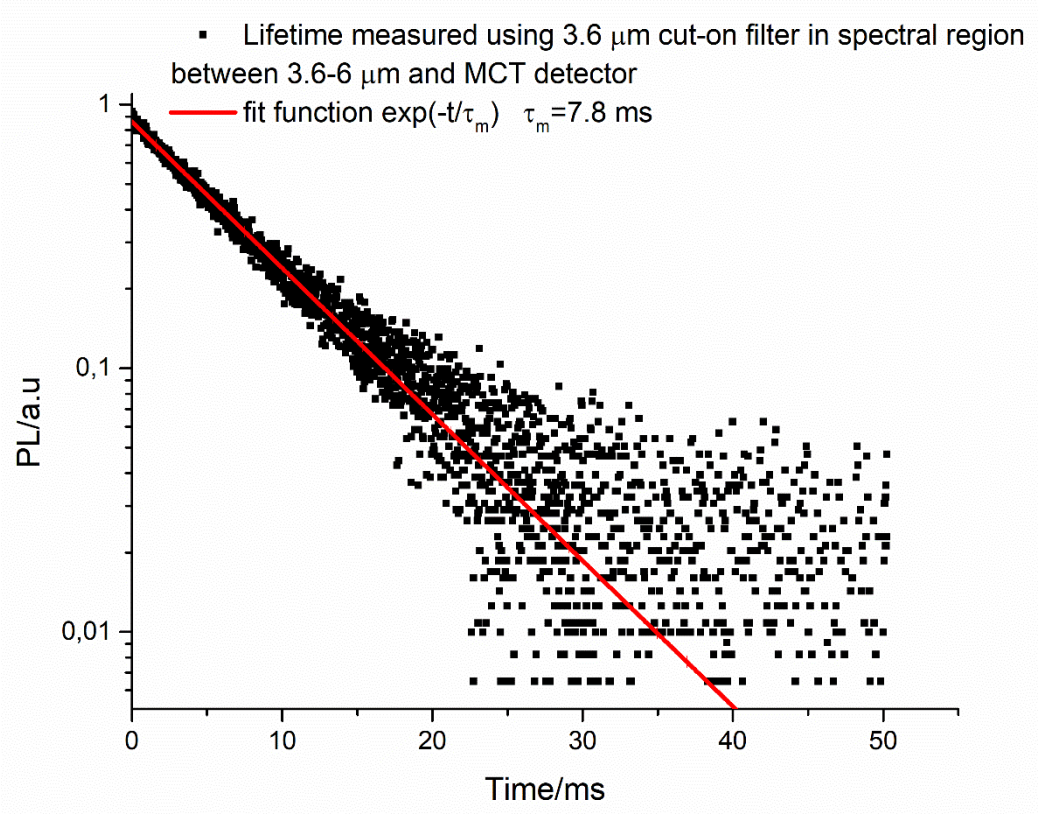

Figure 7. Measured mid-infrared luminescence decay in 500 ppmw Pr^{3+}-doped GeAsGaSe large-core step-index fiber after the laser excitation at 1450 nm. The red plot indicates the best fit to a single exponential function.

4. Numerical Analysis

Using the rate equations' approach, in this section the dependence of the photoluminescence decay is analyzed using a numerical model. The results obtained are compared with the experimental results presented in the previous section. For this purpose, first

the level populations in steady state under pumping into levels $^3F_4$,$^3F_3$ with the 1450 nm pump laser are calculated. This can be accomplished by applying a four level system approximation whereby the levels $^3H_4$ and $^3H_5$ are denoted with indices 1 and 2, respectively while the pairs of levels $^3F_2$,$^3H_6$ and $^3F_4$,$^3F_3$ are denoted with indices 3 and 4, respectively. Following [3], it was assumed that the pairs of levels $^3F_2$,$^3H_6$ and $^3F_4$,$^3F_3$ are in thermal equilibrium and each pair can be effectively treated as a separate level. Thus one obtains a set of four linear algebraic equations:

$$\begin{bmatrix} 1 & 1 & 1 & 1 \\ 0 & a_{22} & a_{23} & a_{24} \\ 0 & 0 & a_{33} & a_{34} \\ a_{41} & 0 & 0 & a_{44} \end{bmatrix} * \begin{bmatrix} N_1 \\ N_2 \\ N_3 \\ N_4 \end{bmatrix} = \begin{bmatrix} N \\ 0 \\ 0 \\ 0 \end{bmatrix} \tag{1}$$

where the matrix elements a_{nn} are given by:

$$\begin{gathered} a_{22} = -\left(\frac{1}{\tau_2} + \frac{1}{\tau_{21mp}}\right); a_{23} = \frac{\beta_{32}}{\tau_3} + \frac{1}{\tau_{32mp}}; \\ a_{24} = \frac{\beta_{42}}{\tau_4}; a_{33} = -\left(\frac{1}{\tau_3} + \frac{1}{\tau_{32mp}}\right); a_{34} = \frac{\beta_{43}}{\tau_4} + \frac{1}{\tau_{43mp}}; \\ a_{41} = \sigma_{a41}\varphi_p; a_{44} = -\left(\sigma_{e41}\varphi_p + \frac{1}{\tau_4} + \frac{1}{\tau_{43mp}}\right); \end{gathered} \tag{2}$$

In (2), σ_{a41} and σ_{e41} are the values of absorption and emission cross sections, respectively, at the pump wavelength. β_{xx} gives the relevant values of the branching ratios. τ_2, τ_3 and τ_4 are radiative lifetimes of levels 2, 3 and 4, respectively, while τ_{xxmp} gives the lifetimes for intrinsic host phonon-assisted transitions and φ_p is the pump photon flux density. Once the initial steady state solution had been calculated, it was used as the initial condition for calculating the time evolution of the photoluminescence decay by solving a set of three coupled ordinary differential equations, which similar to (1) are obtained using the rate equations' approach:

$$\frac{d}{dt}\begin{bmatrix} N_2 \\ N_3 \\ N_4 \end{bmatrix} = \begin{bmatrix} a_{22} & a_{23} & a_{24} \\ 0 & a_{33} & a_{34} \\ -a_{41} & -a_{41} & -a_{41} + a_{44} \end{bmatrix} * \begin{bmatrix} N_2 \\ N_3 \\ N_4 \end{bmatrix} + \begin{bmatrix} 0 \\ 0 \\ a_{41} + N \end{bmatrix} \tag{3}$$

whereby $N_1(t) = N - N_2(t) - N_3(t) - N_4(t)$ and N is the total praseodymium (III) ion doping concentration. The solution of equations (3) forms an initial value problem, which can be solved using standard algorithms for the numerical solution of ordinary differential equations, *cf.* [35].

For the simulations, modelling parameters that have been reported in the available literature were used. The radiative lifetimes of levels 3 and 2 are 4.56 ms and 12.2 ms, respectively [36]. The branching ratio β_{32} is 0.44, while $\beta_{31} = 0.56$. The radiative lifetime of level 4 is 0.22 ms, while the branching ratios used in the simulations are: $\beta_{43} = 0.03$, $\beta_{42} = 0.24$, $\beta_{41} = 0.73$. These numbers were obtained from [33] under the assumption that the radiative transitions from level 4 are dominated by the sublevel $^3F_3$ since approximately 95% of the population of level 4 resides in the sublevel $^3F_3$ according to the Boltzmann distribution [3]. The intrinsic host multi-phonon transition lifetime for each of the levels 4, 3 and 2 is 0.32 ms, 100 ms and 53 ms, respectively. These values were obtained by taking the transition wavelengths given in table 2 of [33], which for levels 4,3 and 2 are respectively 7.4 μm, 4.7 μm and 4.9 μm. The multi-phonon transition rates were calculated using the data provided in [12].

Figure 8 shows the dependence of the numerically calculated dependence of the luminescence intensity for transitions involving levels 4-3, 3-2 and 2-1. The black line shows the sum of the luminescence intensity for all three transitions. The analysis of the energy level diagram of a Pr^{3+}-doped chalcogenide glass host (Fig. 1) suggests that these transitions contribute to the photoluminescence recorded within the MIR wavelength region, *i.e.* from 3.6 μm to 6 μm. The numerically obtained results show that the luminescence originating from transition 2-1 (that is ($^3H_5 \rightarrow {}^3H_4$), see (Fig. 2) clearly is dominant, in agreement with the results shown in Fig. 7, and also with the experimental results reported by other authors, *e.g.* [3]. However, the simulations also show that the luminescence originating from the transition 3-2 ($^3F_2$,$^3H_6 \rightarrow {}^3H_5$) has a non-negligible contribution to the overall luminescence decay. It raises the line above what is predicted by considering solely the transition 2-1 (blue line). A least squares exponential function fit into the results obtained by combining luminescence from all three contributing transitions (($^3F_4$,$^3F_3 \rightarrow {}^3F_2$,$^3H_6$), ($^3F_2$,$^3H_6 \rightarrow {}^3H_5$) and ($^3H_5 \rightarrow {}^3H_4$)) yields an overall photoluminescence lifetime of 8.96 ms. This result is significantly lower than 12.2 ms, stemming from the Judd-Ofelt analysis [36] assumed in the simulations as the level two radiative lifetime. The experimentally obtained lifetime is 7.8 ms (Fig. 7) and is also significantly less than the lifetime predicted by the Judd-Ofelt analysis [36].

Thus, it is concluded that the numerical simulations predict that the lifetime for MIR light calculated numerically within the wavelength range from 3.6 μm to 6 μm is lower than the actual level 2 radiative lifetime. Hence, the experimentally observed lifetime extracted by recording MIR luminescence from 3.6 μm to 6 μm gives only an approximate, lower bound, value of the level 2 radiative lifetime for praseodymium ions.

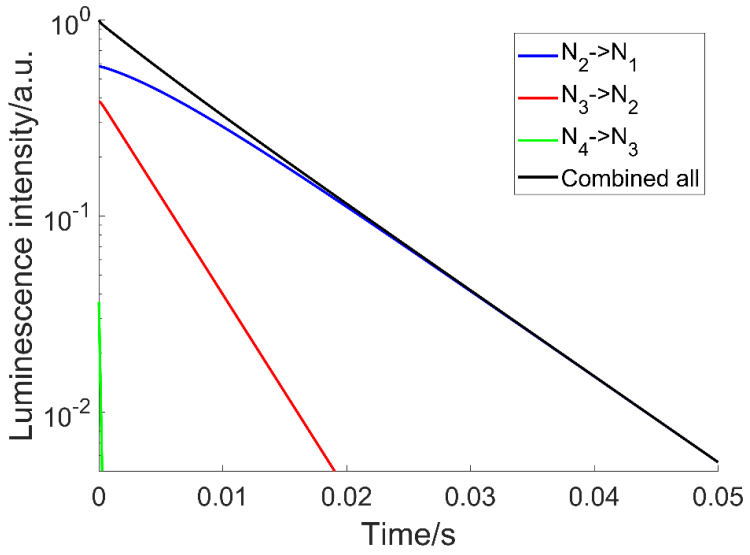

Figure 8. Numerically calculated dependence of luminescence on time, originating from transitions involving levels 4-3, 3-2 and 2-1 (which represent the actual transitions (Fig. 1): ($^3F_4$,$^3F_3 \rightarrow {}^3F_2$,$^3H_6$), ($^3F_2$,$^3H_6 \rightarrow {}^3H_5$) and ($^3H_5 \rightarrow {}^3H_4$), respectively).

Figure 9 shows the numerically calculated dependence of luminescence on time, originating from transitions involving levels 4-2 and 3-1 : (($^3F_4$,$^3F_3 \rightarrow {}^3H_5$) and ($^3F_2$,$^3H_6 \rightarrow {}^3H_4$)). There is a good qualitative agreement of the numerical results with the experimental results shown in Fig. 5. The light contributing to luminescence observed around 2.4 μm thus comes from two transitions (($^3F_4$,$^3F_3 \rightarrow {}^3H_5$) and ($^3F_2$,$^3H_6 \rightarrow {}^3H_4$)) and both of them have a non-negligible contribution. Unlike the luminescent decay presented in Fig. 8, both

transition contributing to luminescence at around 2.4 μm have quite different radiative lifetimes. This results in a fast initial luminescence decay originating from level 4 (($^3F_4$,$^3F_3$ → $^3H_5$), Fig. 1) followed by a much slower luminescent decay originating from level 3 (($^3F_2$,$^3H_6$ → $^3H_4$), Fig. 1). These observations are in full agreement with the experimental results shown in Fig. 5. Also an exponential least squares' fit to extract the lifetimes for both transitions contributing (($^3F_4$,$^3F_3$ → $^3H_5$) and ($^3F_2$,$^3H_6$ → $^3H_4$)) to the luminescence obtained numerically is calculated. This yields 0.130 ms for transition 4-2 (($^3F_4$,$^3F_3$ → $^3H_5$), Fig. 1) and 4.39 ms for the transition 3-1 (($^3F_2$,$^3H_6$ → $^3H_4$), Fig. 1). These numbers differ from the ones obtained experimentally (Fig. 5). Although, the error of 35% for transition 3-1 (($^3F_2$,$^3H_6$ → $^3H_4$), Fig. 1) may be considered within the error bounds of Judd-Ofelt analysis, the error of 45% for the transition 4-2 ($^3F_4$,$^3F_3$ → $^3H_5$), is larger and its explanation may be attributed to a limited accuracy of the multi-phonon transition rate calculation.

To help with understanding of these results, Fig. 10 shows the dependence of the luminescence lifetime for transition 4-2 ($^3F_4$,$^3F_3$ → $^3H_5$), on the multi-phonon lifetime for transition 4-3 ($^3F_4$,$^3F_3$ → $^3F_2$,$^3H_6$). These results confirm that increasing the multiphonon relaxation rate allows obtaining larger values of the luminescence lifetime for transition 4-2 ($^3F_4$,$^3F_3$ → $^3H_5$). Results shown in Fig. 10 suggest also that the multi-phonon lifetime is underestimated. To further stress this point, recalculated results from Fig. 9 using a 4 times larger multi-phonon lifetime for 4-3 transition are shown in Fig. 11. These results quite closely resemble the experimentally observed dependence of the photoluminescence on time shown in Fig. 5.

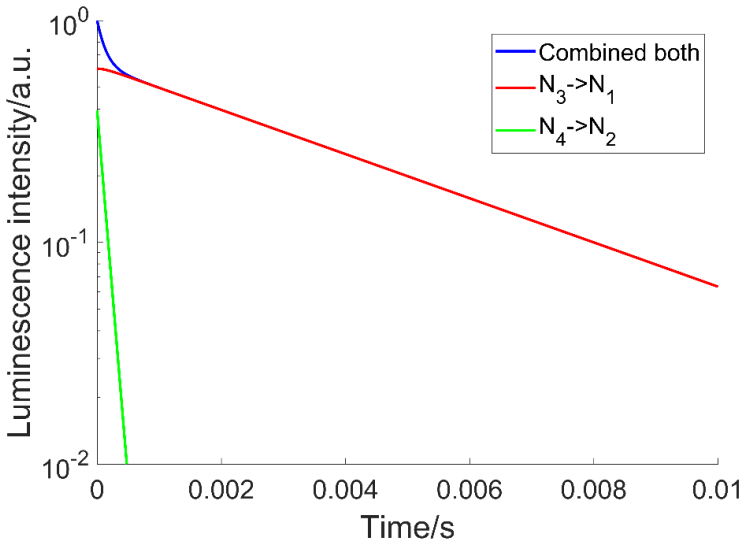

Figure 9. Numerically calculated dependence on time of luminescence originating from transitions involving levels 4-2 and 3-1 (which represent the actual transitions (Fig. 1): ($^3F_4$,$^3F_3$ → $^3H_5$) and ($^3F_2$,$^3H_6$ → $^3H_4$), respectively).

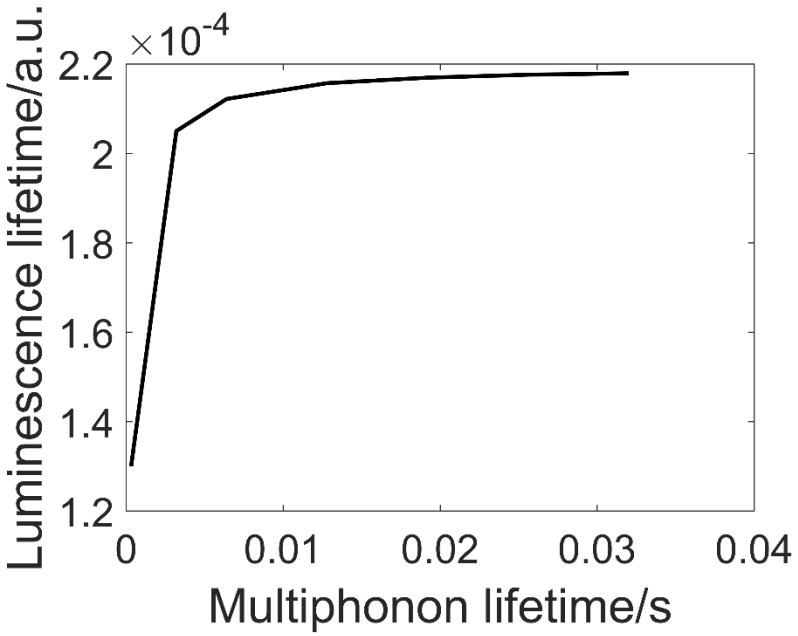

Figure 10. The dependence of the luminescence decay time on the multi-phonon transition lifetime between levels 4 and 3. (which represent the actual transitions (Fig. 1): ($^3F_4$,$^3F_3$ → $^3H_5$), respectively).

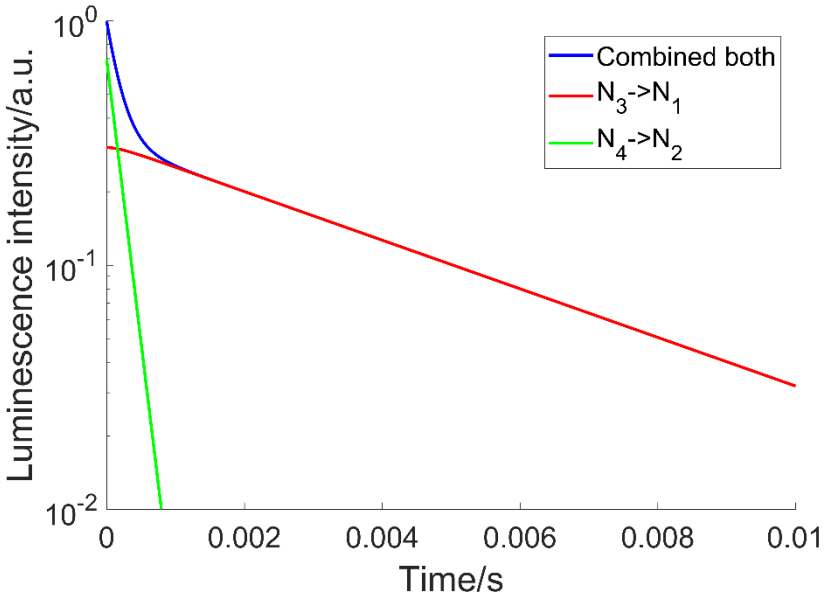

Figure 11. Numerically calculated dependence on time of luminescence originating from transitions involving levels 4-2 and 3-1. (which represent the actual transitions (Fig. 1): ($^3F_4$,$^3F_3$ → $^3H_5$) and ($^3F_2$,$^3H_6$ → $^3H_4$), respectively).

5. Conclusions

In summary, a detailed experimental and numerical analysis of near-infrared and mid-infrared photoluminescence in a Pr^{3+}-doped multi-phonon step-index chalcogenide-selenide glass fiber has been carried out. The numerical results agree qualitatively with the experimental observations and also allow identification of the dominating electronic transitions contributing to the experimentally observed photoluminescence. Importantly, the numerical analysis makes it clear why the observed photoluminescent lifetime within the MIR wavelength range is shorter than that expected from Judd-Ofelt analysis [36]. The numerical results show that apart from the transition ($^3H_5 \rightarrow {}^3H_4$) the transition ($^3F_2, ^3H_6 \rightarrow {}^3H_5$) makes also a significant contribution to MIR luminescence. In addition, the numerical analysis explains the two-exponent near-infrared luminescence decay experimentally observed at ~2.5 μm wavelength. This is because the photoluminescence observed in this wavelength range has contributions from two transitions with differing lifetimes: ($^3F_4, ^3F_3 \rightarrow {}^3H_5$) and ($^3F_2, ^3H_6 \rightarrow {}^3H_4$).

ACKNOWLEDGEMENTS

This project has received funding from the European Union's Horizon 2020 research and innovation programme under the Marie Skłodowska-Curie grant agreement No. 665778 (National Science Centre, Poland, Polonez Fellowship 2016/21/P/ST7/03666). Lukasz Sojka would like to acknowledge support by the Polish Ministry of Science and Higher Education under the project entitled "Iuventus Plus", 2016–2018 (project no. 0441/IP2/2015/73). Krzysztof Anders would like to acknowledge support by the National Science Centre, Poland (grant number 2013/09/N/ST7/04068).

REFERENCES

[1] C. Hughes, M.J. Baker, Can mid-infrared biomedical spectroscopy of cells, fluids and tissue aid improvements in cancer survival? A patient paradigm, Analyst 141 (2015) 467–475. https://doi.org/10.1039/C5AN01858G

[2] J.S. Sanghera, L.B. Shaw, I.D. Aggarwal, Chalcogenide Glass-Fiber-Based Mid-IR Sources and Applications, IEEE J. Sel. Top. Quantum Electron. 15 (2009) 114–119. https://doi.org/10.1109/JSTQE.2008.2010245

[3] L.B. Shaw, B. Cole, P.A. Thielen, J.S. Sanghera, I.D. Aggarwal, Mid-wave IR and long-wave IR laser potential of rare-earth doped chalcogenide glass fiber, IEEE J. Quantum Electron. 37 (2001) 1127–1137. https://doi.org/10.1109/3.945317

[4] G.E. Snopatin, M.F. Churbanov, A.A. Pushkin, V.V. Gerasimenko, E.M. Dianov, V.G. Plotnichenko, High purity arsenic-sulfide glasses and fibers with minimum attenuation of 12 dB/km, Optoelectron. Adv. Mat. 3 (2009) 669–671

[5] J.L. Adam, L. Calvez, J. Troles, V. Nazabal, Chalcogenide Glasses for Infrared Photonics, Int. J. Appl. Glass Sci. 6 (2015) 287–294. https://doi.org/10.1111/ijag.12136

[6] Z.Q. Tang, D. Furniss, M. Fay, H. Sakr, L. Sojka, N. Neate, N. Weston, S. Sujecki, T.M. Benson, A.B. Seddon, Mid-infrared photoluminescence in small-core fiber of praseodymium-ion doped selenide-based chalcogenide glass, Opt. Mater. Express 5 (2015) 870–886. https://doi.org/10.1364/OME.5.000870

[7] M.F. Churbanov, I.V. Scripachev, V.S. Shiryaev, V.G. Plotnichenko, S.V. Smetanin, E.B. Kryukova, Y.N. Pyrkov, B.I. Galagan, Chalcogenide glasses doped with Tb, Dy and Pr ions, J. Non-Cryst. Solids. 326 (2003) 301–305. https://doi.org/10.1016/S0022-3093(03)00417-4

[8] E.R. Barney, Z. Tang, A. Seddon, D. Furniss, S. Sujecki, T. Benson, N. Neate, D. Gianolio, The local environment of Dy^{3+} in selenium-rich chalcogenide glasses. RSC Adv. 4 (2014) 42364–42371. https://doi.org/10.1039/C4RA07192A

[9] H. Sakr, D. Furniss, Z. Tang, L. Sojka, N. A. Moneim, E. Barney, S. Sujecki, T. M. Benson, and A. B. Seddon, Superior photoluminescence (PL) of Pr^{3+} -In, compared to Pr^{3+} -Ga, selenide-chalcogenide bulk glasses and PL of optically-clad fiber, Opt. Express 22 (2014) 21236-21252. https://doi.org/10.1364/OE.22.021236

[10] Z. Tang, N.C. Neate, D. Furniss, S. Sujecki, T.M. Benson, A.B. Seddon, Crystallization behavior of Dy^{3+}-doped selenide glasses, J. Non-Crystal. Solids 357 (2011) 2453–2462. https://doi.org/10.1016/j.jnoncrysol.2010.11.065

[11] H. Sakr, Z.Q. Tang, D. Furniss, L. Sojka, S. Sujecki, T.M. Benson, A.B. Seddon, Promising emission behavior in Pr^{3+}/In selenide-chalcogenide-glass small-core step index fiber (SIF), Opt. Mater. 67 (2017) 98–107. https://doi.org/10.1016/j.optmat.2017.03.034

[12] L. Sojka, Z. Tang, D. Furniss, H. Sakr, Y. Fang, E. Beres-Pawlik, T.M. Benson, A.B. Seddon, S. Sujecki, Mid-infrared emission in Tb^{3+}-doped selenide glass fiber, J. Opt. Soc. Am. B. 34, (2017) A70–A79. https://doi.org/10.1364/JOSAB.34.000A70

[13] S. Sujecki, L. Sojka, E. Beres-Pawlik, H. Sakr, Z. Tang, E. Barney, D. Furniss, T.M. Benson, A.B. Seddon, Numerical modelling of Tb^{3+} doped selenide-chalcogenide multimode fibre based spontaneous emission sources, Opt. Quant. Electron. 49 (2017) 416. https://doi.org/10.1007/s11082-017-1255-5

[14] E.V. Karaksina, V.S. Shiryaev, T.V. Kotereva, M.F. Churbanov, Preparation of high-purity Pr^{3+} doped Ge-Ga-Sb-Se glasses with intensive middle infrared luminescence, J. Lumin. 170 (2016) 37–41. https://doi.org/10.1016/j.jlumin.2015.10.015

[15] E.V. Karaksina, V.S. Shiryaev, M.F. Churbanov, E.A. Anashkina, T.V. Kotereva, G.E. Snopatin, Core-clad Pr(3+)-doped Ga(In)-Ge-As-Se-(I) glass fibers: preparation, investigation, simulation of laser characteristics, Opt. Mater. 72 (2017) 654–660. https://doi.org/10.1016/j.optmat.2017.07.012

[16] V.S. Shiryaev, E.V. Karaksina, T.V. Kotereva, M.F. Churbanov, A.P. Velmuzhov, M.V. Sukhanov, L.A. Ketkova, N.S. Zernova, V.G. Plotnichenko, V.V. Koltashev, Preparation and investigation of Pr^{3+}-doped Ge-Sb-Se-In-I glasses as promising material for active mid-infrared optics, J. Lum. 183 (2017) 129–134. https://doi.org/10.1016/j.jlumin.2016.11.032

[17] L. Bodiou, F. Starecki, J. Lemaitre, V. Nazabal, J.L. Doualan, E. Baudet, R. Chahal, A. Gutierrez-Arroyo, Y. Dumeige, I. Hardy, A. Braud, R. Soulard, P. Camy, P. Nemec, G. Palma, F. Prudenzano, J. Charrier, Mid-infrared guided photoluminescence from integrated Pr^{3+}-doped selenide ridge waveguides, Opt. Mater. 75 (2018) 109–115. https://doi.org/10.1016/j.optmat.2017.10.001

[18] A.B. Seddon, D. Furniss, Z.Q. Tang, L. Sojka, T.M. Benson, R. Caspary, S. Sujecki, True Mid-Infrared Pr^{3+} Absorption Cross-Section in a Selenide-Chalcogenide Host-Glass, 2016 18th International Conference on Transparent Optical Networks (2016)

[19] A.L. Pele, A. Braud, J.L. Doualan, F. Starecki, V. Nazabal, R. Chahal, C. Boussard-Pledel, B. Bureau, R. Moncorge, P. Camy, Dy^{3+} doped GeGaSbS fluorescent fiber at 4.4 μm for optical gas sensing : Comparison of simulation and experiment, Opt. Mater. 61 (2016) 37–44. https://doi.org/10.1016/j.optmat.2016.04.016

[20] F. Starecki, F. Charpentier, J.L. Doualan, L. Quetel, K. Michel, R. Chahal, J. Troles, B. Bureau, A. Braud, P. Camy, V. Moizan, V. Nazabal, Mid-IR optical sensor for CO_2 detection based on fluorescence absorbance of Dy^{3+}:$Ga_5Ge_{20}Sb_{10}S_{65}$ fibers, Sens. Actuators B Chem. 207 (2015) 518–525. https://doi.org/10.1016/j.snb.2014.10.011

[21] F. Starecki, S. Morais, R. Chahal, C. Boussard-Pledel, B. Bureau, F. Palencia, C. Lecoutre, Y. Garrabos, S. Marre, V. Nazabal, IR emitting Dy^{3+} doped chalcogenide fibers for in situ CO_2 monitoring in high pressure microsystems, Int. J. Greenh. Gas Con. 55 (2016) 36–41. https://doi.org/10.1016/j.ijggc.2016.10.015

[22] C.R. Petersen, U. Moller, I. Kubat, B. Zhou, S. Dupont, J. Ramsay, T. Benson, S. Sujecki, N. Abdel-Moneim, Z. Tang, D. Furniss, A.B. Seddon, O. Bang, Mid-infrared supercontinuum covering the 1.4–13.3 μm molecular fingerprint region using ultra-high NA chalcogenide step-index fibre. Nat. Photon. 8 (2014) 830–834. https://doi.org/10.1038/nphoton.2014.213

[23] S. Korsakova, E. Romanova, A. Velmuzhov, T. Kotereva, M. Sukhanov, V. Shiryaev, Peculiarities of the Mid-Infrared Evanescent Wave Spectroscopy Based on Multimode Chalcogenide Fibers, J. Non-Cryst. Solids 475 (2017) 38-43. DOI: https://10.1016/j.jnoncrysol.2017.08.027

[24] E.A. Romanova, S. Korsakova, M. Komanec, T. Nemecek, A. Velmuzhov, M. Sukhanov, V.S. Shiryaev, Multimode Chalcogenide Fibers for Evanescent Wave Sensing in the Mid-IR, IEEE J. Sel. Top. Quantum Electron. 23 (2017) 289–295 https://doi.org/10.1109/JSTQE.2016.2630846

[25] M. El-Amraoui, G. Gadret, J.C. Jules, J. Fatome, C. Fortier, F. Desevedavy, I. Skripatchev, Y. Messaddeq, J. Troles, L. Brilland, W. Gao, T. Suzuki, Y. Ohishi, F. Smektala, Strong infrared spectral broadening in low-loss As-S chalcogenide suspended core microstructured optical fibers, Opt. Express 18 (2010) 26655–26665. https://doi.org/10.1364/OE.18.004547

[26] M.C. Falconi, G. Palma, F. Starecki, V. Nazabal, J. Troles, J.L. Adam, S. Taccheo, M. Ferrari, F. Prudenzano, Dysprosium-Doped Chalcogenide Master Oscillator Power Amplifier (MOPA) for Mid-IR Emission, J. Lightwave Technol. 35 (2017) 265–273. https://doi.org/10.1109/JLT.2016.2632531

[27] M.C. Falconi, G. Palma, F. Starecki, V. Nazabal, J. Troles, J.L. Adam, S. Taccheo, M. Ferrari, F. Prudenzano, Design of an Efficient Pumping Scheme for Mid-IR Dy^{3+}:$Ga_5Ge_{20}Sb_{10}S_{65}$ PCF Fiber Laser, IEEE Photonics Tech. Let. 28, 1984–1987 (2016). https://doi.org/10.1109/LPT.2016.2581022

[28] M.C. Falconi, G. Palma, F. Starecki, V. Nazabal, J. Troles, J.L. Adam, S. Taccheo, M. Ferrari, F. Prudenzano, Novel Pumping Schemes of Mid-IR Photonic Crystal Fiber Lasers for Aerospace Applications, 2016 18th International Conference on Transparent Optical Networks (2016). https://doi.org/10.1109/ICTON.2016.7550623

[29] M.C. Falcni, G. Palma, F. Starecki, V. Nazabal, J. Troles, J.L. Adam, S. Taccheo, M. Ferrari, F. Prudenzano, Recent Advances on Pumping Schemes for Mid-IR PCF Lasers, Proc. SPIE 10100, Optical Components and Materials XIV (2017) 1010002. https://doi.org/10.1117/12.2251710

[30] E.A. Anashkina, A.V. Kim, Numerical Simulation of Ultrashort Mid-IR Pulse Amplification in Praseodymium-Doped Chalcogenide Fibers, J. Lightwave Technol. 35 (2017) 5397–5403. https://doi.org/10.1109/JLT.2017.2775864

[31] E.V. Karaksina, V.S. Shiryaev, T.V. Kotereva, A.P. Velmuzhov, L.A. Ketkova, G.E. Snopatin, Preparation of high-purity Pr^{3+} doped Ge-As-Se-In-I glasses for active mid-infrared optics. J. Lumin. 177 (2016) 275–279. https://doi.org/10.1016/j.jlumin.2016.05.005

[32] A.B. Seddon, Z. Tang, D. Furniss, S. Sujecki, T.M. Benson, Progress in rare-earth-doped mid-infrared fiber lasers, Opt. Express 18 (2010) 26704–26719. https://doi.org/10.1364/OE.18.026704

[33] L. Sojka, Z. Tang, D, Furniss, H. Sakr, A. Oladeji, E. Beres-Pawlik, H. Dantanarayana, E. Faber, A.B. Seddon, T.M. Benson, S. Sujecki, Broadband, mid-infrared emission from Pr^{3+} doped GeAsGaSe chalcogenide fiber, optically clad, Opt. Mater. 36 (2014) 1076-1082. https://doi.org/10.1016/j.optmat.2014.01.038

[34] S. Sujecki, L. Sojka, Z. Tang, D. Jayasuriya, D. Furniss, E. Barney, T. Benson and A. Seddon, Spatiotemporal modeling of mid-infrared photoluminescence from terbium (iii) ion doped chalcogenide-selenide multimode fibers, submitted to J. Rare Earth
[35] W.H. Press, S.A. Teukolsky, W.T. Vetterling, B.P. Flannery, Numerical Recipes in C, second ed., Cambridge University Press, Cambridge, 2002.
[36] L. Sojka, Z. Tang, D. Furniss, H. Sakr, E. Beres-Pawlik, A.B. Seddon, T.M. Benson, S. Sujecki, Numerical and experimental investigation of mid-infrared laser action in resonantly pumped Pr^{3+} doped chalcogenide fibre. Opt. Quant. Electron. 49 (2017) 21. https://doi.org/10.1007/s11082-016-0827-0